

PHOTOMETRIC AND SPECTROSCOPIC STUDIES OF SUPEROUTBURSTS OF THREE DWARF NOVAE
INDEPENDENTLY IDENTIFIED BY THE SVOM/GWAC SYSTEM IN 2018

J. WANG,^{1,2} H. L. LI,² L. P. XIN,² X. H. HAN,² X. M. MENG,² T. G. BRINK,³ H. B. CAI,² Z. G. DAI,⁴
A. V. FILIPPENKO,³ C. -H. HSIA,⁵ L. HUANG,² L. JIA,² G. W. LI,² Y. B. LI,^{6,7,8} E. W. LIANG,¹ X. M. LU,² J. MAO,^{6,7,9}
P. QIU,¹⁰ Y. L. QIU,² J. J. REN,¹⁰ D. TURPIN,² H. J. WANG,¹⁰ X. G. WANG,¹ X. Y. WANG,⁴ C. WU,^{2,8} Y. XU,^{2,8}
J. Z. YAN,¹¹ J. B. ZHANG,¹⁰ W. ZHENG,³ AND J. Y. WEI^{2,8}

- ¹Guangxi Key Laboratory for Relativistic Astrophysics, School of Physical Science and Technology, Guangxi University, Nanning 530004, Peoples Republic of China
²Key Laboratory of Space Astronomy and Technology, National Astronomical Observatories, Chinese Academy of Sciences, Beijing 100101, China
³Department of Astronomy, University of California, Berkeley, CA 94720-3411, USA
⁴School of Astronomy and Space Science, Nanjing University, Nanjing, 210000, China
⁵State Key Laboratory of Lunar and Planetary Sciences, Macau University of Science and Technology, Taipa, Macau, 999078, China
⁶Yunnan Observatories, Chinese Academy of Sciences, Kunming 650011, China
⁷Center for Astronomical Mega-Science, Chinese Academy of Sciences, 20A Datun Road, Chaoyang District, Beijing 100101, China
⁸School of Astronomy and Space Science, University of Chinese Academy of Sciences, Beijing, China
⁹Key Laboratory for the Structure and Evolution of Celestial Objects, Chinese Academy of Sciences, Kunming 650011, China
¹⁰Key Laboratory of Optical Astronomy, National Astronomical Observatories, Chinese Academy of Sciences, Beijing 100101, China
¹¹Purple Mountain Observatory, Chinese Academy of Sciences, Nanjing, 210034, China

(Received July 1, 2016; Revised September 27, 2016; Accepted November 18, 2019)

Submitted to ApJ

ABSTRACT

We report our photometric and spectroscopic follow-up observations of the superoutbursts of three dwarf novae (GWAC 180415A, GWAC 181017A and GWAC 181211A) identified independently by the Ground Wide-angle Cameras system, one of the ground-based instruments of the China-France SVOM mission. Based on a combination of our photometry and that taken from the AAVSO, our period analysis of the superhumps enables us to determine the mass ratios to be 0.0967-0.1163, 0.1879-0.1883 and 0.0981-0.1173 for GWAC 180415A, GWAC 181017A and GWAC 181211A, respectively. GWAC 180415A can be firmly identified as a WZ sge-type dwarf novae due to its long duration (~ 2 weeks) multiple rebrightenings with amplitudes of 3-4 magnitudes, the early superhump associated with a double-wave modulation and the low mass ratio. The inferred low mass ratio and location in the $\varepsilon - P_{\text{orb}}$ diagram suggest that GWAC 181211A is a WZ sge-type dwarf novae candidate. The measured Balmer decrements suggest the Balmer line emission is produced from an optical thick region in GWAC 180415A and GWAC 181017A, and from an optical thin region in GWAC 181211A.

Keywords: stars: dwarf novae — binaries: close — cataclysmic variables — methods: observational — telescopes

Corresponding author: J. Wang
wj@bao.ac.cn

Corresponding author: H. L. Li
lhl@nao.cas.cn

1. INTRODUCTION

Cataclysmic variables (CVs) are semi-detached binaries that consist of a white dwarf (WD, the primary) and a low-mass star (the secondary or donor); see Waner (1995) for a comprehensive review. The secondary is either a low-mass main sequence star or a brown dwarf (BD). An accretion disk is formed around the WD from matter lost by the donor through the inner Lagrangian point, resulting in an outburst due to a thermal instability in the disk (e.g., Meyer & Meyer-Hofmeister 1981; Osaki 1989, 1996; Lasota 2001). Because of their bright outbursts, CVs are important optical transients for on-going and future ground-based time-domain surveys (e.g., Vestrand et al. 2004; Burd et al. 2015; Ivezic et al. 2008; Shappee et al. 2014; Chambers et al. 2016; Wei et al. 2016; Tonry et al. 2018; Graham et al. 2019). For instance, Breedt et al. (2014) released a catalog of 1000 CVs detected by the Catalina Real-Time Transient Survey (CRTS).

With U Geminorum (U Gem) star as a prototype, Dwarf Novae (DNe) having relatively small mass-transfer rate are an important subset of CVs. Based on their outburst phenomena and parameters (e.g., orbital period, outburst amplitude and outburst frequency), there are mainly three sub-types of DNe. Among these, the SU UMa-type DNe exhibit both frequent short outbursts lasting a few days and occasional superoutbursts with a duration of a couple of weeks. The orbital period of the SU UMa-type DNe are typically short, usually below the well-known 2-3 hours period gap (e.g., Ritter & Kolb 2003; Wu et al. 1995). In addition, a superhump with a period longer than the orbital period by a few percent is identified in the SU UMa-type DNe without exception. The superhump is well explained by the dynamical precession of a quasi-elliptic disk due to an expansion beyond the 3:1 resonance radius (e.g., Vogt 1982, Whitehurst 1988, Oskai 1989, Osaki & Kato 2013).

The so-called WZ Sge-type objects are the SU UMa-type DNe with extremely long intervals between superoutbursts that is related to mass transfer (see a comprehensive review by Kato 2015). In contrast to other SU UMa-type DNe, the WZ Sge-type DNe show superoutbursts with amplitudes of 6-8 mag, small mass ratio and extremely short period. Some WZ Sge-type DNe exhibit multiple rebrightenings after a dip (e.g., Imada et al. 2006; Patterson et al. 2002; Meyer & Meyer-Hofmeister 2015). The orbital period of a majority of WZ Sge-type DNe is <0.06 day ($\simeq 87$ minutes), and the mass ratio q is typically smaller than 0.1, which implies a degenerate BD as the companion. In fact, the evolutionary model of CVs predicts that $\sim 40 - 70\%$

of CVs should have a BD companion and have passed the orbital period minimum, i.e., “period bouncer” (e.g., Kolb 1993; Howell et al. 1997; Gansicke et al. 2009; Knigge et al. 2011; Goliasch & Nelson 2015; Pala et al. 2018). This predicted fraction is, however, much larger than the value ($\sim 15\%$) determined from observations (e.g., Savoury et al. 2011), although a few of BD secondary stars have been indeed identified by infrared spectroscopy in some previous studies (e.g., Ciardi et al. 1998; Littlefair et al. 2000, 2003, 2013; Howell & Ciardi 2001; Mennickent et al. 2004; Aviles et al. 2010; Longstaff et al. 2019). A donor with a mass as low as $0.0436 \pm 0.0020 M_{\odot}$ was spectroscopically identified in the eclipsing CV SDSS J105754.25+275947.5 by McAllister et al. (2017). The extreme low mass ratio makes WZ Sge-type DNe special in two ways: 1) the appearance of an inclination-dependent early superhump caused by the 2:1 resonance (e.g., Lin & Papaloizou 1979; Osaki & Myer 2003); and 2) the “period bounce” after passing the period minimum.

Here we report our follow-up photometry and spectroscopy of three DN’s superoutbursts first detected by the ASAS-SN survey (Shappee et al. 2014) but independently identified in 2018 by the Ground Wide-Angle Cameras system (GWAC; Wei et al. 2016; Turpin et al. 2019), enabling us to identify two of them as new WZ Sge-type objects. The paper is organized as follows. Section 2 describes the designation and current status of the GWAC system. The discovery and follow-up observations, along with data reduction, are presented in Sections 3. Sections 4 shows the observational results, paying attention to our period analysis. We discuss the implications in Section 5.

2. GWAC SYSTEM

As one of the ground facilities of SVOM¹, GWAC is designed not only to observe the prompt emission of GRBs in optical bands, but also to independently detect optical transients with a high cadence. The total GWAC system will comprise 36 cameras, covering a total Field-of-View (FoV) of 5400deg^2 , and several additional follow-up telescopes. At the current stage, 16 cameras have been deployed at Xinglong Observatory, National Astronomical Observatories (NAOC). Thanks to the large sky coverage of the system, each GWAC camera is capable of independently searching for optical transients in the sky. Dedicated algorithms were developed to reduce data and to identify triggers

¹ SVOM is a China-France satellite mission dedicated to the detection and study of Gamma-ray bursts (GRBs). Please see White Paper given in Wei et al. (2016) for details.

promptly. The follow-up telescopes that are deployed beside the GWAC cameras include two 60cm telescopes (GWAC-F60A and GWAC-F60B) and one 30cm telescope (GWAC-F30, Xin et al. 2019). The follow-up deep imaging and spectroscopy can be carried out through Target of Opportunity observations by the NAOC 2.16m telescope (Fan et al. 2016) at Xinglong observatory and by the Lijiang 2.4m telescope (LJT) at Gaomeigu observatory. We refer the readers to Appendix for a detailed description of the GWAC system.

3. OBSERVATIONS AND DATA REDUCTION

3.1. *Independent Discovery by GWAC*

The log of the three optical transients, i.e., GWAC 180415A, GWAC 181017A and GWAC 181211A, independently discovered by the GWAC's cameras is presented in Table 1. The UT discovery time is listed in Column (2). Column (7) and (8) respectively give the *G*-band brightness and distance of the quiescent counterparts, extracted from the *Gaia* DR2 catalog (Gaia Collaboration et al. 2018). The typical localization error determined from the GWAC images is about $2''$ in all three cases. The shape of the image profile of the three triggers is very similar to the point-spread-function (PSF) of the nearby bright objects, suggesting with high probability that they are not hot pixels. The three transients did not show any apparent motion among the several consecutive images. There are also no known minor planets or comets within a radius of $15'$. Also, no known variable stars or CVs can be found in SIMBAD around the transient positions within $1'$.

Aperture photometry is carried out for each frame by a dedicated on-line pipeline. The flux calibration was based on the nearby stars listed in the USNO B1.0 catalog. As an illustration, Table 2 shows an example of the photometric results of GWAC 180415A. Column (1) lists the modified Julian date (MJD) at the beginning of the exposure. The calibrated magnitudes in *R*-band and corresponding uncertainties are tabulated in Columns (2) and (3), respectively.

3.2. *Follow-up Photometry and Data Reduction*

We monitored the optical brightness of the three transients in standard Johnson-Bessell *B*, *V*, *R* and *I*-bands by using the GWAC-F60A/B telescopes and the 0.76 m Katzman Automatic Imaging Telescope (KAIT) at Lick Observatory after the discovery. Both GWAC-F60A and GWAC-F60B telescopes, operated jointly by NAOC and Guangxi University, are identical. Each telescope is equipped with an Andor 2048×2048 CCD as a detector mounted at the Cassegrain focus. This setup finally results in a FoV of $19'$.

The exposure times are 20-90 seconds depending on the brightness of the objects, the used filter and the weather condition. The typical seeing was $2\text{-}3''$ during our observations.

Raw images taken with the GWAC-F60A/B telescopes were reduced by following the standard routine in the IRAF² package, including bias and flat-field corrections. The dark-current correction was ignored since its impact on the photometry was negligible once the CCD was cooled down to -60°C .

After standard aperture photometry, absolute photometric calibration was performed based upon several nearby comparison stars whose magnitudes in the Johnson-Cousins system were transformed from the SDSS Data Release 14 catalog through the Lupton (2005) transformation³. An automatic image-reduction pipeline (Ganeshalingam et al. 2010; Stahl et al. 2019), including bias and flat-field corrections and an astrometric solution, was used to reduce the raw images taken by KAIT. PSF photometry was then performed by using the DAOPhot from the IDL Astronomy Users Library.

An example of the follow-up photometry without correction for Galactic extinction is listed in Table 3 for GWAC 180415A. Column (1) lists the MJD at the beginning of the exposure. The filter is given in Column (2). The calibrated magnitudes and the corresponding 1σ uncertainties are tabulated in Columns (3) and (4), respectively. Column (5) lists the used telescope.

3.3. *Follow-up Spectroscopic Observations and Data Reduction*

After the detection of each of the three transients, long-slit spectroscopy was carried out in multiple epochs by the following telescopes: 1) LJT at Yunnan Observatory, 2) NAOC 2.16m telescope at Xinglong Observatory, and 3) Shane 3m telescope at Lick Observatory. A log of the spectroscopic observations is presented in Table 4.

The long-slit spectra taken by LJT use the Yunnan Faint Object Spectrograph and Camera (YFOSC; Fan et al. 2015) that is equipped with a back-illuminated 2048×4096 E2V42-90 CCD as a detector. The grating G14 and a $2.5''$ slit oriented in the south-north direction were used. This setup results in a spectral resolution of $\sim 11\text{\AA}$ as measured from the sky emission lines and comparison lamps, and provides a wavelength coverage

² IRAF is distributed by the National Optical Astronomical Observatories, which are operated by the Association of Universities for Research in Astronomy, Inc., under cooperative agreement with the National Science Foundation.

³ <http://www.sdss.org/dr6/algorithms/sdssUBVRITransform.html#Lupton2005>.

Table 1. Log of the three optical transients independently discovered by the GWAC cameras

ID	UT Time	R.A.	Dec	Other name	Quiescent counterpart	<i>G</i> -band mag	<i>d</i> pc
(1)	(2)	(3)	(4)	(5)	(6)	(7)	(8)
GWAC 20180415A	15:30:19	12:08:57.3	19:16:54	ASASSN-18fk .	SDSS J120857.3+191656.5	19.564 ± 0.005	$340.4^{+112.2}_{-68.2}$
GWAC 20181017A	13:55:00	02:25:06.4	08:06:39	ASASSN-18xt .	AllWISE J022506.37+080638.4	20.190 ± 0.017
GWAC 20181211A	12:34:53	01:48:23.3	-00:48:07	ASASSN-18abn	SDSS J014823.29-004807.4	20.536 ± 0.014	$572.7^{+593.5}_{-269.2}$

Table 2. GWAC photometric results of GWAC180415A in R -band

MJD	Brightness	Error
day	mag	mag
(1)	(2)	(3)
58223.660700	14.81	0.38
58223.662088	14.82	0.43
58223.664345	15.17	0.37
58223.664693	14.87	0.41
58223.666777	14.93	0.38
58223.668512	15.00	0.41
58223.669206	15.22	0.37
58223.669380	15.13	0.37
58223.671811	15.20	0.38
58223.674000	15.26	0.38

Table 3. An example of multi-wavelength photometric results of the follow-up observations of GWAC180415A.

MJD	Filter	Brightness	Error	Telescope
day		mag	mag	
(1)	(2)	(3)	(4)	(5)
58225.245424	B	14.94	0.05	GWAC-F60A
58225.246134	B	15.04	0.05	GWAC-F60A
58225.247553	B	15.00	0.05	GWAC-F60A
58225.248263	B	15.01	0.05	GWAC-F60A
58225.248972	B	14.99	0.05	GWAC-F60A
58225.249681	B	15.11	0.04	GWAC-F60A
58225.250390	B	15.02	0.04	GWAC-F60A
58225.251100	B	15.07	0.04	GWAC-F60A
58225.251809	B	15.09	0.04	GWAC-F60A
58225.276204	B	15.12	0.06	GWAC-F60A

from 3250Å to 7500Å. The wavelength calibration was carried out with the iron-argon comparison lamps.

The long-slit spectra taken with the NAOC 2.16m telescope use either the Optomechanics Research (OMR) Inc. Spectrograph or the Beijing Faint Object Spectrograph and Camera (BFOSC). The OMR spectrograph is equipped with a back-illuminated SPEC 1340×400 pixels CCD as a detector. The grating of 300grooves mm⁻¹ blazed at 6000Å and a slit of a width of 2'' oriented in the south-north direction were used, giving a spectral resolution of ~10Å. Helium-argon comparison lamps were adopted for the wavelength calibra-

Table 4. Log of spectroscopic observations

Transients	Date	Exposure	$\Delta\lambda$	Telescope/Spectrograph
		seconds	Å	
(1)	(2)	(3)	(4)	(5)
GWAC 180415A	2018-04-16UT16:00	750	10	LJT/YFOSC
	2018-04-16UT18:00	900	10	LJT/YFOSC
	2018-04-20	2400	10	2.16m telescope/OMR
	2018-04-23	2400	10	2.16m telescope/OMR
	2018-05-03	1800	2.5	2.16m telescope/BFOSC
GWAC 181017A	2018-10-17	1800	10	2.16m telescope/OMR
GWAC 181211A	2018-12-12	1800	10	2.16m telescope/BFOSC
	2018-12-14	1200	10	2.16m telescope/BFOSC
	2018-12-19	1800	10	2.16m telescope/BFOSC
	2019-01-04	1800	12	Shane telescope/Kast

tions. The BFOSC spectrograph is equipped with a back-illuminated E2V55-30 AIMO CCD. With a slit width of 1.8'' oriented in the south-north direction, the spectral resolutions are ~10Å and ~2.5Å with gratings G4 and G8, respectively. The corresponding wavelength coverage are 3850-8000Å and 5800-8000Å. The wavelength calibrations were carried out with the iron-argon comparison lamps.

The spectrum of GWAC181211A on 4 January 2019 was taken with the Kast spectrograph mounted on the 3m Shane telescope at Lick Observatory. Grism 600/4310 was used on the blue side (1860 s) and grating 300/7500 was used on the red side (1800 s). The slit width was 2'', resulting in a spectral resolution of ~5Å and ~12Å on the blue and red sides, respectively.

All the spectra were obtained as close to meridian as possible, to minimize the effects of atmospheric dispersion. The Lick/Kast slit was oriented along the parallactic angle 209° at an airmass of 1.4. In all but one case, the flux calibrations were carried out with observations of Kitt Peak National Observatory (KPNO) standard stars (Massey et al. 1998); no standard stars were observed on 03 May 2018 when the GWAC180415A spectrum was taken.

Standard procedures were adopted to reduce the two-dimensional spectra using the IRAF package, including bias subtraction and flat-field correction. All of the extracted one-dimensional spectra were then calibrated in wavelength and in flux by the corresponding comparison lamp and standards, except for the GWAC180415A spectrum taken on 03 May 2018. The accuracy of wavelength calibration is better than 1Å for the OMR, YFOSC and Kast spectra, and better than 2Å for the BFOSC spectra. The telluric A-band (7600-7630 Å) and B-band (around 6860Å) features due to O₂ molecules was removed from many (but not all) of the spectra using observations of the corresponding standard.

4. RESULTS AND ANALYSIS

4.1. Photometric light curves

The combined multiwavelength light curves are respectively shown in Figures 1, 2 and 3 for GWAC 180415A, GWAC 181017A and GWAC 181211A. In addition to the photometric results obtained from the GWAC cameras, GWAC-F60A/B telescopes and KAIT, the results extracted from the American Association of Variable Star Observers (AAVSO) website⁴ are also overplotted. When compared to the brightness of the corresponding counterparts in the quiescent state (i.e., Column (7) in Table 1), all three transients reveal a superoutburst with not only an amplitude ≥ 6 mag but also a duration longer than two weeks, typical of WZ Sge-type DNe. The observed superoutburst phenomenon is described for each transient as follows.

4.1.1. GWAC 180415A

The very bright transient ASAS-SN 18fk, with a peak of $V \approx 12$ mag, was reported on 17 March 2018 by the ASAS-SN survey (Shappee et al. 2014). Unfortunately, that sky position was not covered by the GWAC cameras until 15 April 2018. The light curve (Fig. 1) shows a long-duration (~ 2 weeks) rebrightening consisting of several outbursts with an amplitude of 3-4 mag, strongly suggesting that this object is a WZ Sge-type DN. Our observations and resulted light curves are consistent with the study done by Pavlenko et al. (2019). ASAS-SN 18fk has been observed immediately after the discovery by Pavlenko et al. (2019). Their observations were carried out with 18 telescopes located at 15 observatories during 70 nights in unfiltered light. As same as our light curves, their light curve clearly shows six rebrightenings.

4.1.2. GWAC 181017A

This transient with a brightness of 15.59 mag (ASAS-SN 18xt) was first discovered by the ASAS-SN survey on 10 October 2018, earlier than the first detection by the GWAC system by 7 days. The exponential decay is well sampled for this transient by the GWAC-F60A telescope. We do not plot the photometric results given by the GWAC’s cameras because the signal-to-noise ratio (S/N) is marginal for this transient.

4.1.3. GWAC 181211A

A “text-book” light curve, including early raise, power-law decay, and subsequent exponential decay, has been obtained for this transient. The good sampling after the dip by the GWAC-F60A/B telescopes

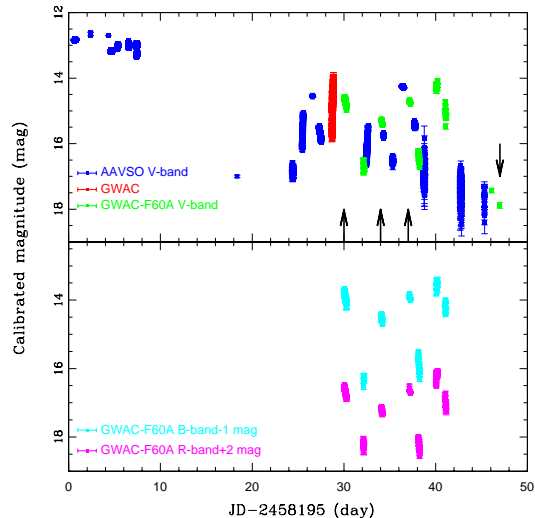


Figure 1. The multi-wavelength light curves of GWAC 180415A since the first detection reported by ASAS-SN survey. All the magnitudes are not corrected for the Galactic extinction. The overplotted vertical arrows mark the epochs when the spectra were obtained by us.

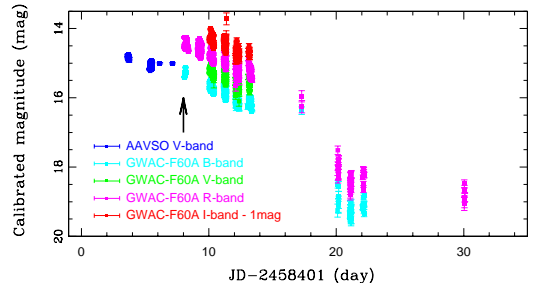


Figure 2. The same as the Figure 1, but for GWAC 181017A.

enable us to firmly exclude an existence of a rebrightening. Thanks to the early monitor by GWAC and GWAC-F60A/B telescopes, the peak amplitude of the superoutburst is inferred to be ~ 6 mag.

4.2. Spectral evolution

The spectral evolution of the three superoutbursts is shown in Figures 4-6. The epochs when these spectra were obtained are marked in Figures 1-3 by the vertical arrows. The blue continuum plus emission and ab-

⁴ <https://www.aavso.org/>.

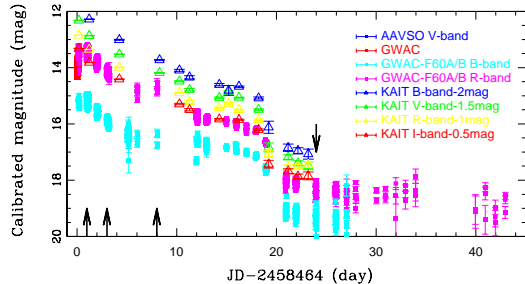


Figure 3. The same as the Figure 1, but for GWAC 181211A.

sorption features are typical of a superoutburst of a DN (e.g., Wu et al. 2001; Baba et al. 2002; Zhao et al. 2006; Sheets et al. 2007; Hiroi et al. 2009; Breedt et al. 2014; Neustroev et al. 2017). The details are described for each DN as follows.

4.2.1. *GWAC 180415A*

The spectra of GWAC 180415A were obtained in its rebrightening phase. A weak and possible double-peaked $H\alpha$ emission line can be identified in all five spectra. The four flux-calibrated spectra are dominated by the high-order broad Balmer absorption lines at the blue end. A transition from emission to absorption is revealed from the line profile of $H\beta$, which clearly shows a broad absorption superposed with a narrow emission profile at the line center. The broad Balmer absorptions and superposed narrow emission lines are believed to be emitted from an optically thick disk and cool gas at the outer disk, respectively (e.g., Clark & Bowyer 1984; Chen & Lin 1989). The $H\alpha$ and $H\beta$ emission line profiles corrected by an absorption line described by a Gaussian function are illustrated in the bottom and middle rows in Figure 7 for two epochs (i.e., 16 and 23 April 2018). Based on the correction of the absorption lines, the Balmer decrements $H\alpha/H\beta$ are measured to be ~ 1.4 and ~ 1.5 ; however, the uncertainties are relatively large because of the low S/N. The flat decrements suggest that the Balmer emission lines are produced in an optically thick accretion disk in the rebrightening stage in GWAC 180415A.

In addition, there are two notches at $\sim 4600\text{\AA}$ and $\sim 5200\text{\AA}$ in the first two spectra taken by LJT/YFOSC on 16 Apr 2018. Although without a convincing iden-

tification, we tentatively identify them as absorptions caused by Fe^+ ions.

There is no detectable He II $\lambda 4686$, He I $\lambda 5016$, He I $\lambda 6678$ or Bowen blend in the spectra. This is quite interesting because Pavlenko et al. (2019) argued that this object is potentially an intermediate polar (IP). The argument of an IP is a strong 22-min brightness modulation that is superimposed on superhumps in only the rebrightening and decline phases which is however inconsistent with the observed spectra. It is known that IPs are typical of strong He II $\lambda 4686$ and Bowen lines (e.g., Neugeruela et al. 2000; Saito et al. 2010). We admit that our spectra were all obtained in the outburst phase. A spectrum taken in quiescent state is helpful for further distinguishing.

4.2.2. *GWAC 181017A*

Only one spectrum was obtained for GWAC 181017A on 17 October 2018. In addition to the $H\alpha$ emission line, the He II $\lambda 4686$ and C III/N III $\lambda\lambda 4634 - 4651$ emission are clearly detected. We measure the $H\alpha/H\beta$ line ratio by direct integration, resulting in a rather flat value of ~ 2.0 . Again, the Balmer emission lines probably come from an optically thick accretion disk. The He II emission line is believed to be produced by a hot chromosphere or coronas above the disk (e.g., Williams 1995; Sarty & Wu 2006).

4.2.3. *GWAC 181211A*

The spectra of GWAC 181211A are typical of a DN. The $H\alpha$ emission line resulting from the accretion disk exhibits a double-peaked profile in three out of the four cases. The He II $\lambda 4686$ and C III/N III $\lambda\lambda 4634 - 4651$ line can be identified in the first two spectra (see the references cited above). The He I $\lambda 5016 + \text{C IV/C III}$ emission can be marginally identified in the first spectrum taken one day after the onset of the superoutburst. The absorption-corrected $H\alpha$ and $H\beta$ emission line profiles are shown in the top row of Figure 7 for the spectrum taken on 12 December 2018. The Balmer decrement is measured to be large, ~ 5.6 , suggesting optically thin condition for the Balmer line-emission region. However, once again, the uncertainty is large because of the low S/N and model-dependent measurement of $H\beta$.

4.3. *Period Analysis*

All three superoutbursts exhibit an ordinary superhump in their light curves, which allows us to perform a period analysis to infer their basic physical parameters. The period analysis is carried out by using the PDM (Stellingwerf 1978) task in the IRAF package.

The left-upper panel in Figure 8 presents the early (< 0.25 day) AAVSO light curve of GWAC 180415A, re-

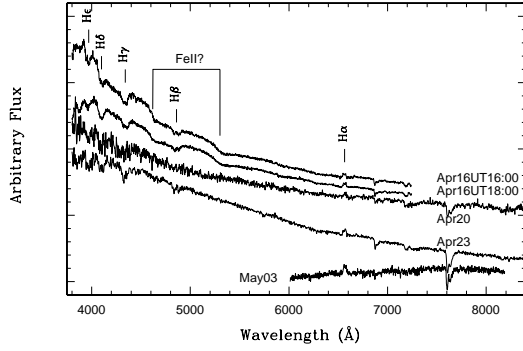


Figure 4. Temporal spectral evolution of the transient GWAC 180415A at the five different epochs from April 16 to May 03, 2018. The spectra are shifted vertically by an arbitrary amount for visibility. The Balmer features, along with the possible Fe II λ 4600 and 5200 features, are marked on the top spectrum.

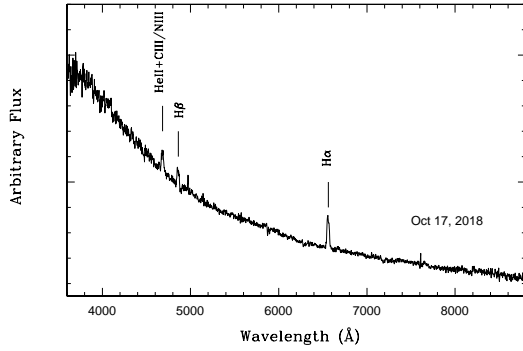


Figure 5. The spectrum of GWAC 181017A taken in October 17, 2018. The Balmer features, along with the He II λ 4686+C III/N III, are marked on the spectrum.

vealing a transition from a raising stage to a declining stage. The upper-right panel shows the derived superhump period, $P = 0.0604$ day. To obtain a more reliable period, we remove the underlying transition by a cubic spline function which is overplotted with the black solid line in the upper-left panel of Figure 8. After removing the underlying transition (the left-lower panel), the su-

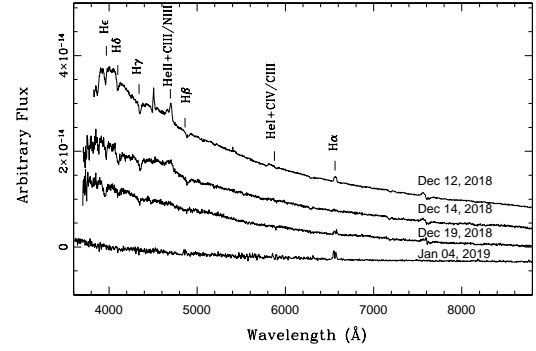


Figure 6. The same as in Figure 4 but for GWAC 181211A. In addition to the Balmer lines, the He II λ 4686+C III/N III and He I λ 5016+C IV/C III features are marked on the top spectrum.

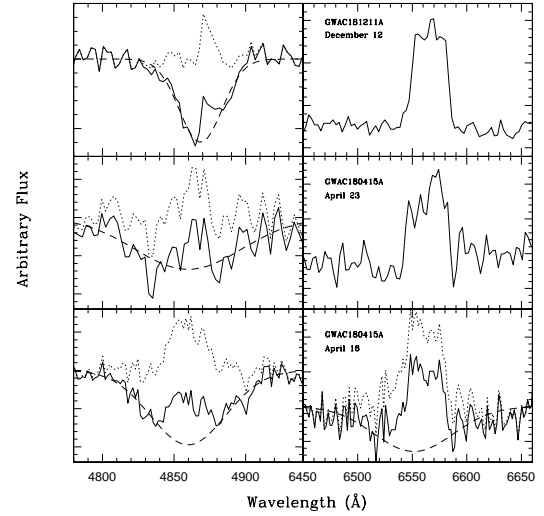


Figure 7. The absorption corrected H β (left panels) and H α (right panels) emission line profiles. In each panel, the observed profile and the modeled Gaussian absorption are plotted by the solid and long dashed lines, respectively. The short dashed line denotes the residual profile after removing the modeled absorption.

perhump period is determined to be $P = 0.0563(1)$ day (the right-lower panel).

The corresponding phase-averaged light curve is shown in the upper panel in Figure 9. One can see from the plot that there is a clear double-wave modulations, typical of the early superhump usually detected in the early raising stage in a WZ Sge-type object (see

Kato 2015 for a review). The existence of an early superhump whose period is extremely close to the orbital period has been, in fact, adopted as a modern definition of WZ Sge-type objects. The early superhump is well understood by the 2:1 resonance that is unique for the binary system with a mass ratio $q < 0.1$ (e.g., Osaki & Myer 2003). The phase-averaged light curve of the ordinary superhump, built from the latter light curve, is plotted in the lower panel in Figure 9. The superhump period of 0.0605 day is highly consistent with the value of 0.057-0.060 days measured by Pavlenko et al. (2019).

Figures 10 and 11 present the phase-averaged light curves of the ordinary superhumps of GWAC 181017A and GWAC 181121A, respectively. For GWAC 181121A, no early superhump period could be measured from the early-time light curve provided by the GWAC’s cameras, although the raising stage has been covered.

The resulted superhump period P_{SH} derived from our period analysis are given in Column (2) in Table 5. Without a measured early superhump period, we estimate the orbital period P_{orb} from the widely used relationship $\varepsilon = -3.3 \times 10^{-2} + 0.84P_{SH}/\text{day}$ (Stolz & Schoembs 1984), where ε is the superhump excess defined as $\varepsilon = (P_{SH} - P_{orb})/P_{orb}$. For each superoutburst, the inferred P_{orb} and ε are listed in the first row of Column (3) and (4) in Table 5, respectively. For GWAC 180415A, the values in brackets are inferred from the double-wave modulation identified in its early-time light curve. Because a few WZ-sge type objects with short P_{orb} and small ε are found to be outliers of the Stolz-Schoembs relationship, the second row presents the corresponding values obtained from a more modern relationship $P_{orb} = 0.91652(52)P_{SH} + 5.39(52)$ given by Gaensicke et al. (2009), where both P_{orb} and P_{SH} are in a unit of minute.

One can see from the table that both relationships return consistent results. Both GWAC 180415A and GWAC 181211A have a small $\varepsilon \sim 0.02$, while a large $\varepsilon \sim 0.04$ can be found for GWAC 181017A. Column (4) lists the mass ratio q that is determined from the empirical relationship $\varepsilon = 0.16q + 0.25q^2$ (Patterson et al. 1998, 2005; Kato et al. 2009; Patterson 2011). Given their similar values of ε , both GWAC 180415A and GWAC 181211A are associated with a $q \approx 0.1$, typical of WZ Sge-type DNe. A larger $q \approx 0.2$ is, however, revealed in GWAC 181017A.

5. DISCUSSION

We report our photometric and spectroscopic monitors of three DN superoutbursts independently detected by the GWAC system in 2018. Based on a combination of our follow-up observations and the data extracted

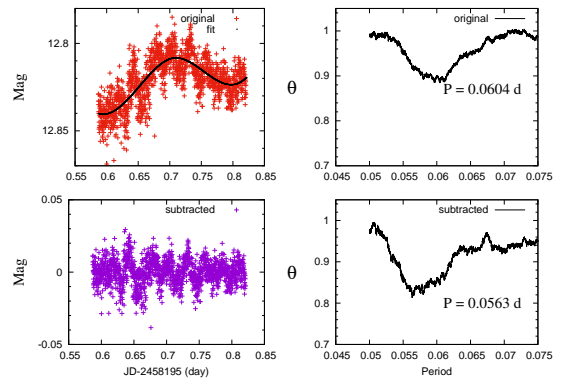


Figure 8. A comparison of the period analysis on the early light curve of GWAC 180415A. The left-upper panel shows the original light curve, and the right-upper panel the corresponding period analysis. The left-lower panel presents the light curve after a fitted sinusoidal function, which is overplotted on the left-upper panel by a solid line, is removed. The corresponding period analysis is illustrated in the right-lower panel.

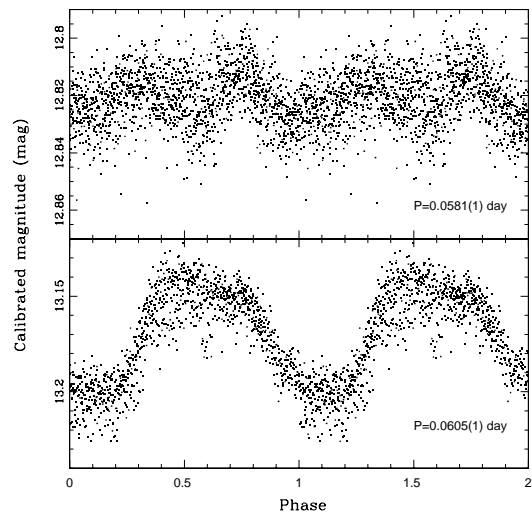


Figure 9. *Upper panel:* the averaged phase plot of the early light curve of GWAC 180415A. *Lower panel:* the same as the upper panel but for the late ordinary superhump.

Table 5. Period analysis of the three superoutbursts

Transients	P_{SH} day	P_{orb} day	ε	q
(1)	(2)	(3)	(4)	(5)
GWAC 180415A	0.0605	0.0594(0.0563)	0.0178(0.0746)	0.0967(0.313)
		0.0592	0.0220	0.1163
GWAC 181017A	0.0800	0.0770	0.0389	0.1879
		0.0770	0.0390	0.1883
GWAC 181211A	0.0598	0.0587	0.0181	0.0981
		0.0585	0.0222	0.1173

from the AAVSO, our period analysis of the associated

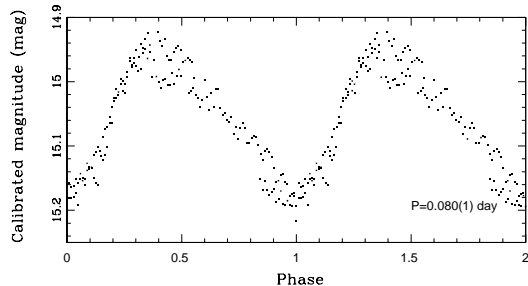


Figure 10. The average phase plot of the superhump of GWAC 181017A.

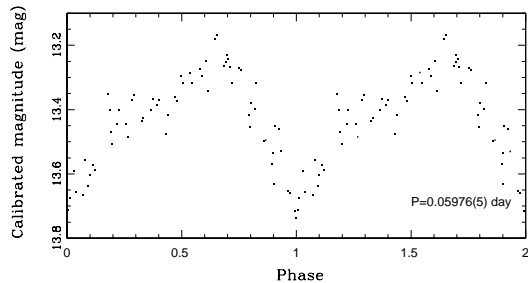


Figure 11. The same as Figure 10 but for GWAC 181211A.

superhumps enables us to identify GWAC 180415A and GWAC 181211A as two new WZ Sge-type objects, both with small values of $\varepsilon < 0.02$ and $q < 0.1$. Relatively large values of $\varepsilon \sim 0.04$ and $q \sim 0.2$ are found to be associated with GWAC 181017A. After correction of the absorption features, a relatively flat Balmer emission-line decrement $H\alpha/H\beta < 2$ is revealed in GWAC 180415A and GWAC 181017A, and a large value of $H\alpha/H\beta = 5.6$ in GWAC 181211A.

Although the normal outburst of a DN can be well understood by the disk instability (e.g., Warner 1995), a different origin is necessary for the superoutburst. Patterson et al. (1981) and Osaki (1985) proposed that

the superoutburst results from enhanced mass transfer; however, this is inconsistent with the early superhump detected in the raising stage (Ishioaka et al. 2002). Osaki & Kato (2013) instead suggests that superoutbursts are caused by a thermal-tidal instability with constant mass transfer. A model with either an extremely low- α (< 0.003) or a magnetically truncated disk is required to reproduce the long burst interval observed in the WZ Sge-type DNe,

We argue that the identification of GWAC 180415A as a WZ Sge-type DN is additionally supported by several observed rebrightenings with a total duration of about two weeks, although the exact mechanism of the rebrightening is still under debate. Proposed mechanisms include an enhanced α value due to magnetohydrodynamics (e.g., Osaki et al. 2001), accretion of the matter beyond the 3:1 resonance (e.g., Kato et al. 1998), and repeat reflections of transverse waves in the disk (e.g., Meyer & Meyer-Hofmeister 2015).

We estimate the mass of the secondary star in the three DNe from the inferred corresponding mass ratio q . The mean mass of WD (M_{WD}) is $0.81 \pm 0.04 M_{\odot}$ in CVs (Savory et al. 2011), and $0.621 M_{\odot}$ in the field SDSS magnitude-limited WD sample (Tremblay et al. 2016). With a range of $0.6 M_{\odot} \leq M_{\text{WD}} \leq 0.8 M_{\odot}$, the mass of the secondary is inferred to be $0.058 M_{\odot} \leq M_2 \leq 0.094 M_{\odot}$, $0.113 M_{\odot} \leq M_2 \leq 0.153 M_{\odot}$, and $0.073 M_{\odot} \leq M_2 \leq 0.095 M_{\odot}$ for GWAC 180415A, GWAC 181017A and GWAC 181211A, respectively. Given the inferred masses of the secondary, we could not entirely exclude an existence of a BD in GWAC 180415A and GWAC 181211A.

The possible existence of a BD secondary in GWAC 180415A is further supported by the detection of the quiescent counterpart in the IR by WISE (Cutri et al. 2013, and references therein), although a contamination by a foreground or background source cannot be entirely excluded because of the low spatial resolution of WISE. Among the four IR bands, the object is detected only in the first two short bands: $w1(3.4\mu\text{m}) = 17.17 \pm 0.13$ mag and $w2(4.6\mu\text{m}) = 16.22 \pm 0.20$ mag, implying an extremely red IR color of $w1 - w2 = 0.95$ mag. There are no measurements in the J -, H -, and K -bands.

We first model the ultraviolet (UV) through IR spectral energy distribution (SED) of the quiescent counterpart of GWAC 180415A by a linear combination of two blackbodies through χ^2 minimization, deriving a WD temperature of $T_1 = 11,400 \pm 500\text{K}$ and a companion temperature of $T_2 = 950 \pm 40\text{K}$; see Figure 12. The resulted reduced χ^2 is 2.16 for 9 data points and 4 free parameters. We additionally model the SED by the theoretical grid of spectra of a pure hydrogen atmosphere

given by Tremblay & Bergeron (2009). The surface gravity is fixed to be $\log g = 8.0$ (cgs unit) in our modeling, which is the typical value of $\log g$ of the modeled atmospheric parameters of nearby WDs (Giammichele et al. 2012). We at first fit the SED and calculate the corresponding χ^2 statistics for a series of theoretical spectra with fixed effective temperature T_{eff} . The matching is based on only the UV and optical bands. The best match with the lowest χ^2 returns a consistent WD temperature $T_{\text{eff}} = 11,000\text{K}$. With the determined temperature and the assumed surface gravity, the WD mass is inferred to be $0.603M_{\odot}$ from the DA model grid calculated by Tremblay et al. (2011), suggesting a mass of the secondary of $0.058M_{\odot}$.

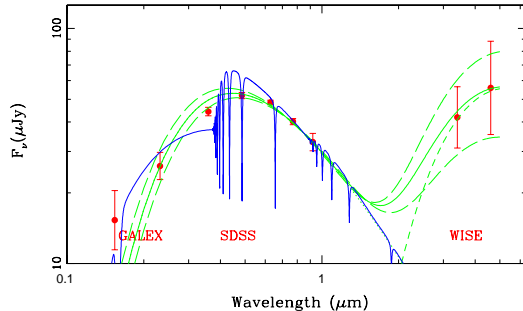


Figure 12. The multi-wavelength SED (the red points) of SDSS J120857.3+191656.5, the quiescent counterpart of GWAC 180415A, from FUV to infrared. The data are extracted from Galex (Martin et al. 2005), SDSS (Abazajian et al. 2009) and WISE (Cutri et al. 2013). The green solid and dashed lines show the best fit by a linear combination of two blackbodies and the corresponding 1σ confidence level. The blue line is the best fit theoretical spectrum with a temperature of $T = 11,000\text{K}$ that is extracted from the pure hydrogen grid built by Tremblay & Bergeron (2009).

For the quiescent counterpart of GWAC 181211A, we model the corresponding SDSS DR14 spectrum by the same theoretical spectral grid by the same method. The surface gravity is again fixed to be $\log g = 8.0$ since the modeling is found to be insensitive to the value of $\log g$ because of the poor S/N, which means there are only two free parameters. By ignoring the weak emission at the line centers of $\text{H}\alpha$ and $\text{H}\beta$ in the fitting, the best fit shows that the observed spectrum can be well reproduced by a model spectrum with $T = 10,000\text{K}$, shown

in Figure 13. The WD mass is therefore inferred to be $0.6M_{\odot}$ through the same method, suggesting a mass of the secondary of $0.059M_{\odot}$.

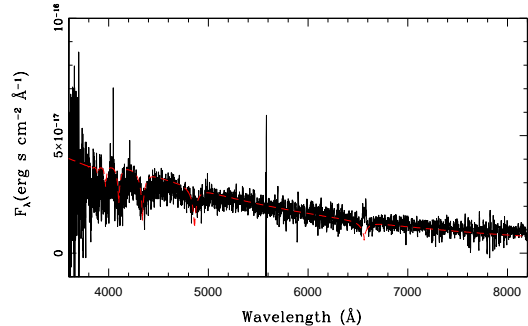


Figure 13. An illustration of the modeling of the SDSS DR14 spectrum of SDSS J014823.29-004807.4, the quiescent counterpart of GWAC 181211A. The observed spectrum and the best fit DA model with a temperature of $T = 10,000\text{K}$ are shown by the black solid and red dashed curves, respectively.

Figure 14 shows the $P_{\text{orb}} - \varepsilon(q)$ diagram that is a powerful tool for describing the evolution of a CV (e.g., Howell et al. 2001). Comparison of the observations and the theoretical evolution track with a $M_{\text{WD}} = 0.75M_{\odot}$ given by Knigge et al. (2011) confirms that both GWAC 180415A and GWAC 181211A are WZ Sge-type objects close to the period minimum because the locations of the two superoutbursts coincide with those of the previously confirmed WZ Sge-type objects. The comparison suggests that GWAC 181017A is a prebouncer system. We argue that this result is further supported by the detection of the quiescent counterpart by WISE. The quiescent counterpart of GWAC 181017A has $w1(3.4\mu\text{m}) = 17.19 \pm 0.13$ mag and $w2(4.6\mu\text{m}) = 17.29 \pm 0.54$ mag, giving an IR color of $w1 - w2 = -0.1$ mag. This color differs from that of GWAC 180415A significantly, implying a more massive secondary in GWAC 181017A than in GWAC 180415A. By extracting it from the Pan-STARRS1 surveys catalog (Chambers et al. 2016), the more massive secondary can be additionally inferred from its red color, $r - i = 0.31$ mag.

6. CONCLUSION

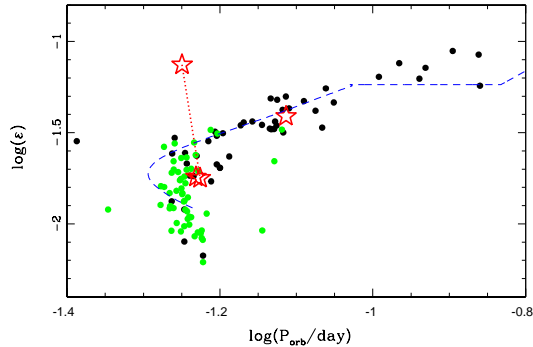


Figure 14. The $\varepsilon - P_{\text{orb}}$ diagram. The red stars mark the positions of the three superoutbursts studied in this paper. The two stars connected with a dashed line denotes the two measurements of GWAC 180415A. One is based on the periods of both early light curve and late ordinary superhump, and the another on the ordinary superhump period only. The black dots denote the pre-bouncer systems given in Patterson (2011), and the green ones the confirmed WZ Sge-type DNe taken from Kato (2015). The dashed blue line is the theoretically predicted evolutionary track of a CV with a WD mass of $0.75M_{\odot}$ provided in Kingge et al. (2011).

We report photometric and spectroscopic follow-up observations of the superoutbursts of three DNe (GWAC 180415A, GWAC 181017A and GWAC 181211A) that were identified independently by ASAS-SN and the Ground Wide-angle Cameras system. The mass ratios estimated from the period analysis of the ordinary superhumps are 0.0967-0.1163, 0.1879-0.1883 and 0.0981-0.1173 for GWAC 180415A, GWAC 181017A and GWAC 181211A (respectively). GWAC 180415A shows not only long duration (~ 2 weeks) multiple rebrightenings with an amplitude of about 3-4 magnitudes, but also an early superhump associated with a double-wave modulation, which indicates a firm identification of the object as a WZ sge-type DNe. GWAC 181211A is a WZ sge-type DNe candidate taking into account of its small mass ratio. The measured Balmer decrements suggest the Balmer line emission is produced from an optical thick region in GWAC 180415A and GWAC 181017A, and from an optical thin region in GWAC 181211A.

The authors thank the anonymous referee for his/her careful review and helpful suggestions that improved the

manuscript. The study is supported by the National Basic Research Program of China (grant 2014CB845800), the NSFC under grants 11533003, and the Strategic Pioneer Program on Space Science, Chinese Academy of Sciences, grant Nos. XDA15052600 & XDA15016500. JW is supported by the National Natural Science Foundation of China under grant 11773036, by Natural Science Foundation of Guangxi (2018GXNSFGA281007), and by Bagui Young Scholars Program, JM is supported by the NSFC grants 11673062, the Hundred Talent Program of Chinese Academy of Sciences, the Major Program of Chinese Academy of Sciences (KJZD-EW-M06), and the Oversea Talent Program of Yunnan Province. Special thanks go to the staff at Xinglong Observatory as a part of National Astronomical Observatories, China Academy of Sciences for their instrumental and observational help. This study is supported by the Open Project Program of the Key Laboratory of Optical Astronomy, NAOC, CAS. The GWAC system is partially funded by National Astronomical Observatories, CAS, and the Guangxi Key Laboratory for Relativistic Astrophysics. This study used the SDSS archive data that was created and distributed by the Alfred P. Sloan Foundation, the Participating Institutions, the National Science Foundation, and the U.S. Department of Energy Office of Science. This study uses the data collected by Wide-field Infrared Survey Explorer (WISE), which is a joint project of the University of California, Los Angeles, and the Jet Propulsion Laboratory/California Institute of Technology, funded by the National Aeronautics and Space Administration. This study uses the data obtained by GALEX, which is a NASA Small Explorer, and uses the NASA/IPAC Extragalactic Database (NED), which is operated by the Jet Propulsion Laboratory, California Institute of Technology, under contract with NASA. This work has made use of data from the European Space Agency (ESA) mission *Gaia* (<https://www.cosmos.esa.int/gaia>), processed by the *Gaia* Data Processing and Analysis Consortium (DPAC, <https://www.cosmos.esa.int/web/gaia/dpac/consortium>). Funding for the DPAC has been provided by national institutions, in particular the institutions participating in the *Gaia* Multilateral Agreement.

Facilities: Ground Wide-Angle Cameras (GWAC), GWAC-F60A/B telescope, Xinglong Observatory 2.16m telescope, Lijiang 2.4m telescope (LJT), Shane 3m telescope, 0.76 m Katzman Automatic Imaging Telescope (KAIT)

Software: IRAF (Tody 1986, 1993), Python, IDL

APPENDIX

A. DESIGNATION OF GWAC SYSTEM

A refractive telescope with an effective aperture size of 18 cm is adopted for each camera. A field corrector composed of 8 lenses is designed for each camera to correct the comet aberration at the edge of the FoV. The f -ratio is $f/1.2$ for each camera, resulting in a FoV of 150deg^2 and a spatial resolution of $11.7''\cdot\text{pixel}^{-1}$ when each of the cameras is equipped with a 4096×4096 E2V back-illuminated CCD chip operating in the 0.5 to 0.85 μm band. All the CCDs with a full well of about $10^5 e^-$ are operated at a gain of about $2e^- \text{ADU}^{-1}$. The readout noise is $13e^- \text{pixel}^{-1}$ for each chip when the readout time is set to 5 seconds. The thermoelectric coolers can keep the CCDs at a temperature of -50°C , which is acceptable because at this temperature the noise of a broad-band and large-area sky survey is mainly contributed by the sky background rather than the dark current. No filters are used in order to have a relatively deep detection capability. In a 10 s exposure, limiting magnitudes of $m_V = 15$ and $m_V = 16 \text{mag}^5$ can be reached at a significance of 5σ during full moon and new moon, respectively, and the cameras saturate for objects brighter than $m_V = 11 \text{mag}$.

The GWAC cameras adopt a German equatorial mount tracking in both axes, a superior choice for an all-sky survey. Each mount carries four cameras (called a “unit” of the GWAC system) pointing to different sky areas, so the total FoV of each unit is $\sim 600 \text{deg}^2$. The maximum slew velocity of the mounts is 1.5°s^{-1} for both axes. The tracking accuracy over 5 minutes is better than $2''$ at the zenith. A closed loop based on the astrometry of the detected stars is used to guarantee high tracking accuracy during a long-duration observation.

B. SURVEY STRATEGY

As a start point, we divide the whole sky into several grids having equivalent areas that correspond to the FoV of one GWAC unit. In the survey, each GWAC unit is assigned to a given grid. The monitor duration is from half an hour to as long as six hours for an individual grid. When making the observing schedule, the grids with a Galactic latitude of $b < 20^\circ$ are avoided, since the extremely high star density in the GWAC images greatly reduces the detection efficiency of any transient. During the survey, a minimum angular distance from the center of each grid to the Moon is necessary for avoiding both strong sky background and bright stray light recorded in the GWAC images. The minimum distance depends on the lunar phase: 30° when the phase is less than 0.5, 40° when the phase is 0.5-0.75, and 40° when the phase is >0.75 .

Based on the catalog cross-match method, a dedicated real-time transient detection pipeline has been developed for the GWAC system. Briefly, all the point sources detected in each GWAC image are compared to a reference catalog to find transient candidates. The reference catalog is produced by combining the constantly updated local GWAC catalog and the available catalogs provided by other whole sky surveys such as the USNO B1.0. The local GWAC catalog is built from stacked, high-quality reference images taken by the GWAC system in advance. This strategy based on a combination of catalogs has advantages. On the one hand, the public astronomical catalogs are static, which would result in heavy pollution from false positives such as the known long-term variable stars (e.g., Mira variable stars). On the other hand, although the false positive issue can be somewhat addressed by the local GWAC catalog, the completeness of the catalog is reduced in some cases. For example, some faint objects around very bright stars are difficult to be found in the GWAC images with low spatial resolution, and they are consequently excluded from the local GWAC catalog.

We note that the combination of the local GWAC catalog and the archive catalogs must be finely tuned, since the density of stars in each field is different. A list of proper and auto-adapted parameters should be set to ensure that the used reference catalog not only is complete at the sensitivity limit of the GWAC cameras, but also does not contain too many redundant faint objects. For the GWAC system, the reference images and the reference catalog are updated as long as new images with higher quality are obtained.

In addition to real optical transients, the transient candidates detected by the GWAC detection pipeline include asteroids, meteors, satellites, comets, airplanes, hot pixels, dust on the mirror or CCD, and image defects. Algorithms are involved in our pipeline to filter out these false-positives and contamination. Some of them, such as satellites, can be efficiently removed by analyzing a series of more than two consecutive images. A pipeline based on machine-learning

⁵ The white-band magnitude can be well calibrated and transformed to the R -band in the Johnson system. In order to be consistent with the requirement of GWAC system presented in the white paper (Wei et al. 2016), the corresponding V -band magnitude is obtained by transforming from the calibrated R -band magnitude by assuming a spectrum of a G-type star.

algorithm has been developed to filter out the variable hot pixels and dust (Xu et al. in preparation). For slowly moving objects (e.g., minor planets), custom-developed software has been running in the local database to predict the positions and brightnesses for all the known minor planets. The prediction can be cross-matched with the observed sky position of a transient candidate in real time when a new alert is generated. The accuracy of this dedicated software are better than 0.5', which has been checked with the predictions given by MPC⁶ on-line.

REFERENCES

- Abazajian, K. N., Adelman-McCarthy, J. K., Agueros, M. A., et al. 2009, *ApJS*, 182, 543
- Aviles, A., Zharikov, S., & Tovmassian, G. 2010, *ApJ*, 711, 389
- Baba, H., Sadakane, K., Norimoto, Y., et al. 2002, *PASJ*, 54, L7
- Breedt, E., Gansicke, B. T., Drake, A. J., et al. 2014, *MNRAS*, 443, 3174
- Burd, A., Cwiok, M., Czyrkowski, H., et al. 2015, *NewA*, 10, 409
- Chambers, K. C., Magnier, E. A., Metcalfe, N., et al. 2016, *arXiv:astro-ph/1612.05560*
- Ciardi, D. R., Howell, S. B., Hauschildt, P. H., et al. 1998, *ApJ*, 504, 450
- Cutri, R. M., et al. 2013, *yCat*, 2328
- Fan, Yu-Feng, Bai, Jin-Ming, Zhang, Ju-Jia, Wang, Chuan-Jun, Chang, Liang, Xin, Yu-Xin, & Zhang, Rui-Long 2015, *RAA*, 15, 918
- Fan, Z., Wang, H. J., Jiang, X. J., et al. *PASP*, 128, 5005
- Gaia Collaboration, et al. 2018, *A&A*, 616, 1
- Ganeshalingam, M., Li, W. D., Filippenko, A. V., et al. 2010, *ApJS*, 190, 418
- Gansicke, B. T., Dillon, M., Southworth, J., et al. 2009, *MNRAS*, 397, 2170
- Goliasch, J. & Nelson, L. 2015, *ApJ*, 809, 80
- Graham, M. J., Kulkarni, S. R., Bellm, E. C., et al. 2019, *PASP*, 131, 1001
- Hiroi, K., Moritani, Y., Nogami, D., et al. 2009, *PASJ*, 61, 697
- Howell, S. B., & Ciardi, D. R. 2001, *ApJL*, 550, 57
- Howell, S. B., Rappaport, S., & Politano, M. 1997, *MNRAS*, 287, 929
- Howell, S. B., Nelson, L. A., & Rappaport, S. 2001, *ApJ*, 550, 897
- Imada, A., Kubota, K., Kato, T., et al. 2006, *PASJ*, 58, L23
- Ishioka, R., Uemura, M., Matsumoto, K., et al. 2002, *A&A*, 381, L41
- Ivezic, Z., Axelrod, T., Becker, A. C., et al. 2008, *AIP Conference Proceedings*, 1082, 359
- Kato, T. 2015, *PASJ*, 67, 108
- Kato, T., Imada, A., Uemura, M., et al. 2009, *PASJ*, 61, 395
- Kato, T., Pavlenko, E. P., Maehara, H., 2009, *PASJ*, 61, 601
- Kato, T., Maehara, H., Miller, I., et al. 2012, *PASJ*, 64, 21
- Kato, T., Nogami, D., Masuda, S., & Baba, H. 1998, *PASP*, 110, 1400
- Kolb, U. 1993, *A&A*, 271, 149
- Knigge, C., Baraffe, I., & Patterson, J. 2011, *ApJS*, 194, 28
- Kulkarni, S. R. 2018, *ATel*, 11266, 1
- Lasota, J. -P. 2001, *NewAR*, 45, 449
- Longstaff, E. S., Casewell, S. L., Wynn, G. A., Page, K. L., Williams, P. K. G., Braker, I., & Maxted, P. F. L. 2019, *MNRAS*, 484, 2566
- Lin, D. N. C., & Papaloizou, J. 1979, *MNRAS*, 186, 799
- Littlefair, S. P., Dhillon, V. S., Howell, S. B., & Ciardi, D. R. 2000, *MNRAS*, 313, 117
- Littlefair, S. P., Dhillon, V. S., & Martn, E. L. 2003, *MNRAS*, 340, 264
- Littlefair, S. P., Savoury, C. D. J., Dhillon, V. S., et al. 2013, *MNRAS*, 431, 2820
- Martin, D. C., Fanson, J., Schiminovich, D., et al. 2005, *ApJL*, 619, 1
- Massey, P., Strobel, K., Barnes, J. V., et al. 1988, *ApJ*, 328, 315
- McAllister, M. J., Littlefair, S. P., Dhillon, V. S., et al. 2017, *MNRAS*, 467, 1024
- Mennickent, R. E., Diaz, M. P., & Tappert, C. 2004, *MNRAS*, 347, 1180
- Meyer, F., & Meyer-Hofmeister, E. 1981, *A&A*, 104, L10
- Meyer, F., & Meyer-Hofmeister, E. 2015, *PASJ*, 67, 52
- Negueruela, I., Reig, P., & Clark, J. S. 2000, *A&A*, 345, L29
- Neustroev, V. V., Marsh, T. R., Zharikov, S. V., et al. 2017, *MNRAS*, 467, 597
- Osaki, Y. 1985, *A&A*, 144, 369
- Osaki, Y. 1989, *PASJ*, 41, 1005
- Osaki, Y. 1996, *PASP*, 108, 39
- Osaki, Y., & Kato, T. 2013, *PASJ*, 65, 95
- Osaki, Y., & Meyer, F. 2003, *A&A*, 401, 325
- Osaki, Y., Meyer, F., & Meyer-Hofmeister, E. 2001, *A&A*, 370, 488
- Pala, A. F., Schmidtbreick, L., Tappert, C., et al. 2018, *MNRAS*, 481, 2523
- Patterson, J. 2011, *AAS*, 21810303

⁶ <https://www.minorplanetcenter.net/>

- Patterson, J., Kemp, J., Harvey, D. A., et al. 2005, *PASP*, 117, 1204
- Patterson, J., Masi, G., Richmond, M. W., et al. 2002, *PASP*, 114, 721
- Patterson, J., McGraw, J. T., Coleman, L., & Africano, J. L. 1981, *ApJ*, 248, 1067
- Patterson, J., Richman, H., Kemp, J., & Mukai, K. 1998, *PASP*, 110, 403
- Ritter, H., & Kolb, U. 2003, *A&A*, 404, 301
- Savoury, C. D. J., Littlefair, S. P., Dhillon, V. S., et al. 2011, *MNRAS*, 415, 2025
- Shappee, B., Prieto, J., Stanek, K. Z., et al. 2014, *AAS*, 223, 23603
- Sheets, H. A., Thorstensen, J. R., Peters, C. J., & Kapusta, A. B. 2007, *PASP*, 119, 494
- Sarty, G. E., & Wu, K. 2006, *PASA*, 23, 106
- Stahl, B., Zheng, W., de Jaeger, T., et al., 2019, [arXiv:1909.11140](https://arxiv.org/abs/1909.11140)
- Stolz, B., & Schoembs, R. 1984, *A&A*, 132, 187
- Stellingwerf, R. F. 1978, *ApJ*, 221, 661
- Tody, D. 1986, *Proc. SPIE*, 627, 733
- Tody, D. 1993, in *ASP Conf. Ser.* 52, *adass II*, ed. R. J. Tonry, J. L., Denneau, L., Heinze, A. N., et al. 2018, *PASP*, 130, 4505
- Tremblay, P. -E., & Bergeron, P. 2009, *ApJ*, 696, 1755
- Tremblay, P. -E., Bergeron, P., & Gianninas, A. 2011, *ApJ*, 730, 128
- Tremblay, P. -E., Cummings, J., Kalirai, J. S., Gansicke, B. T., Gentile-Fusillo, N., & Raddi, R. 2016, *MNRAS*, 461, 2100
- Turpin, D., Wu, C., Han, X. H., et al. 2019, *RAA* submitted, [arXiv:astro-ph/1902.08476](https://arxiv.org/abs/1902.08476)
- Vestrand, W. T., Borozdin, K. N., Brumby, S. P., et al. 2004, *SPIE*, 4845, 126
- Vogt, N. 1982, *ApJ*, 252, 653
- Warner, B. 1995, *Cataclysmic Variable Stars*, Cambridge Astrophysical Ser. 28; Cambridge Univ. Press, Cambridge
- Wei, J. Y., Cordier, B., et al. 2016, [arXiv:astro-ph/1610.0689](https://arxiv.org/abs/1610.0689)
- Whitehurst, R. 1988, *MNRAS*, 232, 35
- Williams, G. A., 1995, *AJ*, 109, 319
- Wu, X. A., Li, A. Y., & Gao, W. H. 2001, *ApJL*, 549, 81
- Wu, K., Wickramasinghe, D. T., & Warner, B. 1995, *PASA*, 12, 60
- Zhao, Y. H., Li, Z. Y., Wu, X. A., & Peng, Q. H. 2006, *AJ*, 131, 1667